https://doi.org/10.5194/gmd-2023-189
Preprint. Discussion started: 24 October 2023
© Author(s) 2023. CC BY 4.0 License.

Geoscientific Model Development Discussions

Modelling chemical advection during magma ascent

Hugo Dominguez [1], Nicolas Riel [2], and Pierre Lanari [1]

[1]Institute of Geological Sciences, University of Bern, Baltzestrasse 1+3, CH-3012 Bern, Switzerland
[2]Institute of Geosciences, Johannes Gutenberg-University, Mainz, Germany

Correspondence: Hugo Dominguez (hugo.dominguez@unibe.ch)

Abstract.

Modelling magma transport requires robust numerical schemes for chemical advection. Current numerical schemes vary in their ability to be mass conservative, computationally efficient, and accurate. This study compares four of the most commonly used numerical schemes for advection: an upwind scheme, a weighted essentially non-oscillatory (WENO-5) scheme, a semi-Lagrangian (SL) scheme, and a marker-in-cell (MIC) method. We assess the behaviour of these schemes using the passive advection of two different magmatic compositions. This is coupled in 2D with the temporal evolution of a melt anomaly that generates porosity waves. All algorithms, except the upwind scheme, are able to predict the melt composition with reasonable accuracy. In terms of total running time, the upwind and SL schemes are the fastest, and the MIC scheme is the slowest. The WENO-5 scheme shows intermediate total running time but has the lowest amount of mass loss and therefore is best suited for this problem.

1 Introduction

Mechanisms of magma ascent and emplacement within the lithosphere and upper asthenosphere remain largely unconstrained (e.g., Connolly and Podladchikov, 2007b; Katz et al., 2022). Studies have attempted to address this problem using techniques ranging from geophysical measurements of the present-day lithosphere to geochemical analysis of the rock record . However, geophysical studies are hampered by indirect measurements, and natural samples in geochemical studies represent only the end-product of the melting processes (Brown, 2013; Clemens et al., 2022; Johnson et al., 2021). Comparatively, numerical modelling allows investigation of these processes at a range of scales in space and time (e.g., Keller, 2013; Katz and Weatherley, 2012).

To numerically model such open systems, it is necessary to be able to describe the chemical and physical processes responsible for magma ascent in a rock. At low melt fractions and in the absence of externally applied stress, the physical processes are based on the continuum formulation of two-phase flow. It takes into account the concurrent mechanisms of rock matrix compaction and buoyancy of partial melt in an interconnected porous network (e.g., Scott and Stevenson, 1984; McKenzie, 1984). This formulation is based on mass and momentum conservation, and an appropriate set of constitutive relationships. In addition, conservation of energy needs to be ensured to link mechanical to chemical processes (e.g., Katz, 2008). Chemical processes, such as phase reactions, can be considered using thermodynamics and/or kinetics and relate the equilibration of the melt with the hosting rock (e.g., Omlin et al., 2017; Bessat et al., 2022). They contribute to the transport dynamics by changing

https://doi.org/10.5194/gmd-2023-189
Preprint. Discussion started: 24 October 2023
© Author(s) 2023. CC BY 4.0 License.

Geoscientific Model Development Discussions
Open Access
EGU

rock properties, such as density, viscosity, porosity and permeability (Jha et al., 1994; Aharonov et al., 1995b; Keller and Katz, 2016). However, the amount of melt interacting with the rock is also modulated by transport mechanisms (Kelemen et al., 1997; Spiegelman and Kenyon, 1992; Aharonov et al., 1995a). Therefore, the development of integrated models that successfully describe the complex interaction between reaction and transport is key to understanding melting and melt extraction at all scales.

Numerous numerical studies have investigated reactive melt transport. It has been shown that melts that partially crystallise or dissolve the host rock could be a viable mechanism for channelling flow and creating heterogeneities in the mantle, in the context of oceanic middle ridges (Aharonov et al., 1997; Spiegelman et al., 2001) and sub-arc mantle (Bouilhol et al., 2011). Concerning lower crust melting, this approach has mainly been used to understand the processes of chemical differentiation and the compositional range of magma in mafic systems (e.g., Jackson et al., 2005; Solano et al., 2012; Riel et al., 2019).

One challenge of reactive melt transport modelling is the advection of the melt composition through its ascent. This part, which is mathematically trivial as it is described by a simple mass balance equation, is numerically challenging (e.g., LeVeque, 1992). This is mainly due to the fact that most numerical models are based on an Eulerian frame of reference, where the discretised space is fixed in space and in time. In contrast, transport is by essence better defined from a Lagrangian perspective, where the observer follows the particles of fluid as they move. In addition, two-phase flow models are at least 2D problems due to the formation of channels (e.g., Barcilon and Lovera, 1989; Connolly and Podladchikov, 2007b) and to the fact that mass cannot be transported efficiently in 1D in the melt (Jordan et al., 2018). This brings limitation to the resolution of the models and hence requires accurate advection schemes.

This study compares four numerical schemes applied to the problem of the advection of magmatic composition: an upwind scheme, a weighted essentially non-oscillatory (WENO) scheme, a semi-Lagrangian (SL) scheme and a marker-in-cell (MIC) method. This selection provides a good representation of the different approaches to solving advection problems that are commonly used in a wide range of applications. We assess the performance of each scheme in terms of accuracy, mass conservation and computational time. A 2D model that couples chemical advection with a two-phase flow solver is then used to evaluate which algorithm is best suited to this problem.

2 Governing equations

Chemical transport in two-phase flow systems is described by the four mass conservation equations of the system (e.g., Aharonov et al., 1997). The first two equations describe the conservation of the total mass of the solid and the liquid:

$$\frac{\partial\left[(1-\phi)\rho_{\mathrm{s}}\right]}{\partial t} = -\nabla\cdot\left[(1-\phi)\boldsymbol{v_{\mathrm{s}}}\rho_{\mathrm{s}}\right], \tag{1}$$

$$\frac{\partial(\phi\rho_{\mathrm{f}})}{\partial t} = -\nabla\cdot\left(\phi\boldsymbol{v_{\mathrm{f}}}\rho_{\mathrm{f}}\right), \tag{2}$$

https://doi.org/10.5194/gmd-2023-189
Preprint. Discussion started: 24 October 2023
© Author(s) 2023. CC BY 4.0 License.

Geoscientific Model Development Discussions

where f and s are the fluid and solid phases, t is the time (in s), ϕ is the fluid-filled porosity, ρ, the density of the respective phase ($\mathrm{kg.s^{-3}}$), $\boldsymbol{v}$, the velocity of the respective phase ($\mathrm{m.s^{-1}}$). The last two equations express the conservation of each chemical component within the solid and fluid phases:

$$\frac{\partial\left[(1-\phi)\rho_{\mathrm{s}}C_e^{\mathrm{s}}\right]}{\partial t} = \nabla\cdot\left[D_e^{\mathrm{s}}(1-\phi)\rho_{\mathrm{s}}\nabla C_e^{\mathrm{s}} - (1-\phi)\boldsymbol{v_{\mathrm{s}}}\rho_{\mathrm{s}}C_e^{\mathrm{s}}\right], \tag{3}$$

$$\frac{\partial\left(\phi\rho_{\mathrm{f}}C_e^{\mathrm{f}}\right)}{\partial t} = \nabla\cdot\left(\mathbf{D_e^f}\phi\rho_{\mathrm{f}}\nabla C_e^{\mathrm{f}} - \phi\boldsymbol{v_{\mathrm{f}}}\rho_{\mathrm{f}}C_e^{\mathrm{f}}\right), \tag{4}$$

where C_e is the mass fraction of the component e in the respective phase, D_e^{s} is the solid diffusion coefficient of the component e (in $\mathrm{m^2.s^{-1}}$) and $\mathbf{D_e^f}$, the hydrodynamic dispersion tensor of the component e in the fluid ($\mathrm{m^2.s^{-1}}$). These four equations assume no mass transfer due to reactions between the solid and the liquid phases.

2.1 Simplifications

In this study, the advection of the chemical components transported by the liquid phase is considered and the diffusion term in Eqs. (3) and (4) is neglected. Since $\rho_{\mathbf{s}}$ is assumed to be constant and that the host rock has a fixed composition, Eq. (3) is omitted.

Subtracting Eq. (2) in Eq. (4), and dividing by ρ_{f} and ϕ yields:

$$\frac{\partial(C_e^{\mathrm{f}})}{\partial t} = -\boldsymbol{v_{\mathrm{f}}}\nabla\cdot(C_e^{\mathrm{f}}). \tag{5}$$

Equation (5) is formally equivalent to Eq. (4) without the dispersion term. Moreover, Eq. (4) is written in conservative form, whereas Eq. (5) is expressed in Lagrangian or non-conservative form. In addition, Eq. (5) removes the time dependence on ϕ.

An expression for $\boldsymbol{v_{\mathrm{f}}}$ can be derived by coupling Eqs. (1) and (2) to the momentum conservation equations (e.g., McKenzie, 1984; Bercovici et al., 2001). These are usually solved before Eq. (5) ; a description of the system used in this study is provided below in section 4.1.

2.1.1 Numerical Methods

Solving an advection equation using a linear Eulerian scheme leads to high numerical diffusion for first-order schemes, such as the upwind scheme (Courant et al., 1952), and to oscillations on sharp gradients for higher-order schemes (LeVeque, 2002). The latter effect is described by Godunov's theorem (Godunov and Bohachevsky, 1959). This theorem states that linear Eulerian schemes of order of accuracy greater than one cannot preserve the monotonicity of the solution for sharp gradients, discontinuities or shocks. This has led to extensive developments in the design of high-order Eulerian non-linear schemes that can achieve high accuracy without bringing oscillations. Examples of such developments are the essentially non-oscillatory (ENO) methods (Harten et al., 1987), that later led to weighted essentially non-oscillatory (WENO) schemes (Liu et al., 1994).

https://doi.org/10.5194/gmd-2023-189
Preprint. Discussion started: 24 October 2023
© Author(s) 2023. CC BY 4.0 License.

Geoscientific Model Development Discussions

These schemes are based on the idea of using a non-linear adaptive procedure to automatically choose the locally smoothest stencil and earlier examples of applications include the modelling of shocks appearing in acoustics (e.g., Grasso and Pirozzoli, 2000) or solving the Hamilton-Jacobi equations (e.g., Jiang and Peng, 2000).

Another approach is to use schemes closer to Lagrangian perspective, such as the Marker-In-Cell (MIC) (or alternatively named Marker-And-Cell) method (e.g., Harlow et al., 1955; Gerya and Yuen, 2003a). It consists ~~at~~ tracking individual particles on a Lagrangian frame and ~~to reinterpolate~~ them when needed on an Eulerian stationary ~~mesh grid.~~ This approach has the advantage of producing little numerical diffusion and ~~to be~~ uncondionnally stable and has been ~~used extensively~~ ~~to advect most fields~~ in geodynamics, ~~such as physical properties and compositions~~ (e.g., Gerya, 2019; van Keken et al., 1997; Duretz et al., 2011).

Finally, there are intermediate methods, such as semi-Lagrangian methods, trying to take advantages from both Eulerian and Lagrangian schemes (Robert, 1981; McDonald, 1984). These schemes look at different particles at each timestep, considering only particles whose final trajectories correspond to the position of a fixed Eulerian grid. This has the advantage of only considering a number of particles equal to the resolution of the Eulerian grid and is computationally efficient. They are also unconditionally stable, but have issues with mass conservation (Chandrasekar, 2022). They were first developed for atmospheric modelling (e.g., Robert, 1981; Staniforth and Côté, 1991) and later successfully used in the plasma modelling community (e.g., Sonnendrücker et al., 1999).

To solve for Eq. (5) in the context of two-phase flow, we implement and test four different advection schemes that are representative of the approaches described above: an upwind scheme, a WENO scheme, a SL scheme and a MIC method.

2.2 Upwind scheme

The upwind scheme is among the simplest algorithm for solving an advection equation on an Eulerian grid (e.g., LeVeque, 1992). It is explicit and first-order in space and in time. It consists of using a spatially biased stencil that depends on the direction of the flow (Fig. 1).

2.2.1 Spatial discretization

Using a first-order biased spacial stencil, Eq. (5) can be approximated for 1 element and in 1D as:

$$\begin{aligned} \frac{\partial C_i}{\partial t} + v_{\mathrm{f},i} \frac{C_i^n - C_{i-1}^n}{\Delta x} = 0 \quad \text{for} \quad v_{\mathrm{f},i} > 0, \\ \frac{\partial C_i}{\partial t} + v_{\mathrm{f},i} \frac{C_{i+1}^n - C_i^n}{\Delta x} = 0 \quad \text{for} \quad v_{\mathrm{f},i} < 0, \end{aligned} \tag{6}$$

where i is a spatial index in the x direction and Δx is a constant increment in space.

2.2.2 Temporal discretization

Combined with the first-order forward Euler method, we retrieve the classical upwind scheme from Eq. (6):

https://doi.org/10.5194/gmd-2023-189
Preprint. Discussion started: 24 October 2023
© Author(s) 2023. CC BY 4.0 License.

Geoscientific Model Development Discussions
Open Access
EGU

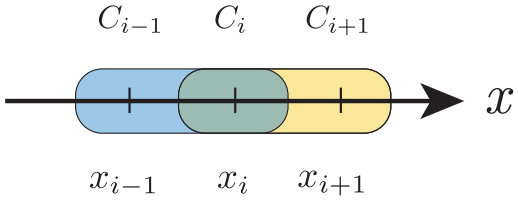

Figure 1. Spatial stencil of the Upwind scheme in 1D. The blue box is the valid stencil for positive velocities and the yellow box for negative velocities.

$$\begin{aligned} &\frac{C_i^{n+1} - C_i^n}{\Delta t} + v_{\mathrm{f},i} \frac{C_i^n - C_{i-1}^n}{\Delta x} = 0 \quad \text{for} \quad v_{\mathrm{f},i} > 0, \\ &\frac{C_i^{n+1} - C_i^n}{\Delta t} + v_{\mathrm{f},i} \frac{C_{i+1}^n - C_i^n}{\Delta x} = 0 \quad \text{for} \quad v_{\mathrm{f},i} < 0, \end{aligned} \tag{7}$$

where Δt is the timestep.

It can also be rewritten in a more compact form:

$$C_i^{n+1} = C_i^n - \Delta t \left[v_{\mathrm{f},i}^+ \left(\frac{C_i^n - C_{i-1}^n}{\Delta x} \right) + v_{\mathrm{f},i}^- \left(\frac{C_{i+1}^n - C_i^n}{\Delta x} \right) \right], \tag{8}$$

where

$$v_{\mathrm{f},i}^+ = \max(v_{\mathrm{f},i}, 0),$$
$$v_{\mathrm{f},i}^- = \min(v_{\mathrm{f},i}, 0).$$

This scheme is well known to produce a lot of numerical diffusion and is bounded by the following Courant–Friedrichs–Lewy (CFL) condition, for p dimensions:

$$\Delta t \left(\sum_{j=1}^{p} \frac{|v_{\mathrm{f}_j}|}{\Delta x_j} \right) \leq C_{\max} = 1, \tag{9}$$

where $C_{\max}$ is the maximum Courant number (e.g., Hirsch, 2007).

2.3 Weighted essentially non-oscillatory scheme

Weighted Essentially Non-Oscillatory schemes (WENO) were developed by Liu et al. (1994). The reader can refer to Shu (2009) for a comprehensive review of the development of WENO schemes and Pawar and San (2019) for implementations using ~~Julia.~~

https://doi.org/10.5194/gmd-2023-189
Preprint. Discussion started: 24 October 2023
© Author(s) 2023. CC BY 4.0 License.

Geoscientific Model Development Discussions

They are high order schemes able to resolve sharp gradient, produce little numerical diffusion but also follow the same CFL condition as the ~~Upwind~~ scheme. The key idea behind them, is to use a non-linear adaptive procedure to automatically choose the locally smoothest stencil. This allow WENO schemes to dispose of oscillations when advecting sharp gradients.

We use a 5th order in space finite-difference approach for non-conservative ~~problem,~~ referenced as WENO-5 hereafter.

2.3.1 Spatial Discretization

Equation (5) can be discretized in space using WENO-5 scheme similarly to the upwind scheme, in 1D and for ~~1~~ element such as:

$$\frac{\partial C_i}{\partial t} + v_{f,i}^{+}\left(\frac{C_{i+\frac{1}{2}}^{L} - C_{i-\frac{1}{2}}^{L}}{\Delta x}\right) + v_{f,i}^{-}\left(\frac{C_{i+\frac{1}{2}}^{R} - C_{i-\frac{1}{2}}^{R}}{\Delta x}\right) = 0, \tag{10}$$

where

$$\begin{aligned} C_{i+\frac{1}{2}}^{L} = {} & w_0^L\left(\frac{1}{3}C_{i-2} - \frac{7}{6}C_{i-1} + \frac{11}{6}C_i\right) + \\ & w_1^L\left(-\frac{1}{6}C_{i-1} + \frac{5}{6}C_i + \frac{1}{3}C_{i+1}\right) + \\ & w_2^L\left(\frac{1}{3}C_i + \frac{5}{6}C_{i+1} - \frac{1}{6}C_{i+2}\right), \\ C_{i-\frac{1}{2}}^{R} = {} & w_0^R\left(-\frac{1}{6}C_{i-2} + \frac{5}{6}C_{i-1} + \frac{1}{3}C_i\right) + \\ & w_1^R\left(\frac{1}{3}C_{i-1} + \frac{5}{6}C_i - \frac{1}{6}C_{i+1}\right) + \\ & w_2^R\left(\frac{11}{6}C_i - \frac{7}{6}C_{i+1} + \frac{1}{3}C_{i+2}\right). \end{aligned}$$

Here, $C_{i-\frac{1}{2}}^{L}$ and $C_{i+\frac{1}{2}}^{R}$ are omitted to avoid redundancy. They can be obtained by shifting the index by -1 and 1 respectively. ~~N~~on-linear weights w are defined as:

$$w_k^L = \frac{\alpha_k}{\alpha_0 + \alpha_1 + \alpha_2}, \quad \alpha_k = \frac{d_k^L}{(\beta_k + \epsilon)^2}, \quad k = 0,1,2$$
$$w_k^R = \frac{\alpha_k}{\alpha_0 + \alpha_1 + \alpha_2}, \quad \alpha_k = \frac{d_k^R}{(\beta_k + \epsilon)^2}. \quad k = 0,1,2$$

The values of the optimal weights d_k^L and d_k^R are given in Table 1 and ϵ is fixed at 1×10^{-6} to avoid division by zero. Smoothness indicators β are equal to:

https://doi.org/10.5194/gmd-2023-189
Preprint. Discussion started: 24 October 2023
© Author(s) 2023. CC BY 4.0 License.

Geoscientific Model Development Discussions
Open Access
EGU

Table 1. Optimal weights for WENO-5 scheme

d_k	k=0	k=1	k=2
d_k^L	0.1	0.6	0.3
d_k^R	0.3	0.6	0.1

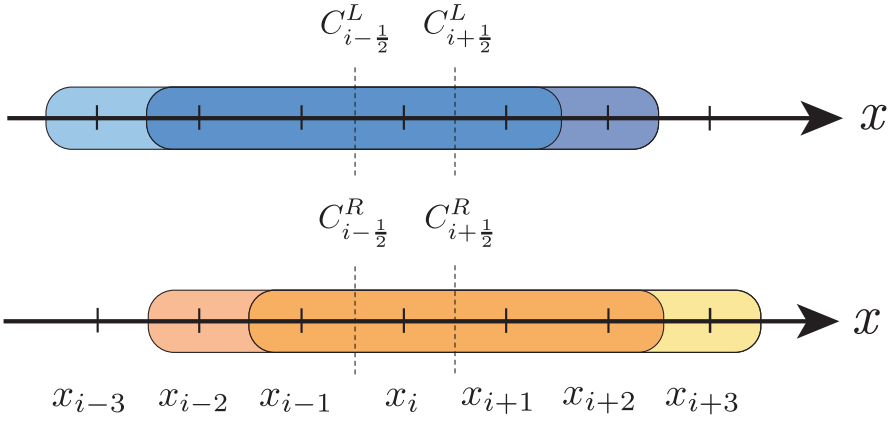

Figure 2. Spatial stencil of the WENO-5 scheme in 1D. C^L is used for positive velocities and C^R for negative velocities. The blue boxes are valid stencils for positive velocities and the yellow and orange boxes are valid for negative velocities.

$$\beta_0 = \frac{13}{12}\left(C_{i-2} - 2C_{i-1} + C_i\right)^2 + \frac{1}{4}\left(C_{i-2} - 4C_{i-1} + 3C_i\right)^2,$$

$$\beta_1 = \frac{13}{12}\left(C_{i-1} - 2C_i + C_{i+1}\right)^2 + \frac{1}{4}\left(C_{i-1} - C_{i+1}\right)^2,$$

$$\beta_2 = \frac{13}{12}\left(C_i - 2C_{i+1} + C_{i+2}\right)^2 + \frac{1}{4}\left(3C_i - 4C_{i+1} + 3C_{i+2}\right)^2.$$

WENO-5 in 1D requires a stencil of 5 points biased towards the left for positive velocities and 5 points biased towards the right for negative velocities as shown on Fig. 2. Careful consideration must then be given to boundary conditions for complex problems.

2.3.2 Temporal discretization

WENO schemes are not stable using the standard forward Euler time integration method (Wang and Spiteri, 2007). The most commonly used discretisation is the third-order Strong Stability Preserving (SSP) explicit Runge-Kutta method (e.g., Jiang and Shu, 1996; Ghosh and Baeder, 2012). SSP schemes are used to fully capture discontinuous solutions and are therefore very useful for solving hyperbolic partial differential equations (Gottlieb et al., 2001).

https://doi.org/10.5194/gmd-2023-189
Preprint. Discussion started: 24 October 2023
© Author(s) 2023. CC BY 4.0 License.

Geoscientific Model Development Discussions

The third-order SSP Runge-Kutta for Eq. (5) for 1 element can be written as:

$$C_i^1 = C_i^n - \Delta t L(C_i^n), \tag{11}$$

$$C_i^2 = \frac{3}{4}C_i^n + \frac{1}{4}\left[C_i^1 - \Delta t L\left(C_i^1\right)\right], \tag{12}$$

$$C_i^{n+1} = \frac{1}{3}C_i^n + \frac{2}{3}\left[C_i^2 - \Delta t L\left(C_i^2\right)\right], \tag{13}$$

with L being the spacial discretization operator:

$$L(C_i) = v_{\mathrm{f},i}^{+}\left(\frac{C_{i+\frac{1}{2}}^L - C_{i-\frac{1}{2}}^L}{\Delta x}\right) + v_{\mathrm{f},i}^{-}\left(\frac{C_{i+\frac{1}{2}}^R - C_{i-\frac{1}{2}}^R}{\Delta x}\right).$$

With this formulation, the WENO-5 scheme is fifth order in space and third order in time.

2.4 Semi-Lagrangian schemes

Semi-Lagrangian (SL) schemes take a different approach than classical Eulerian methods and are related to tracer-based advection schemes. SL schemes aim to use the best of Lagrangian and Eulerian methods by solving the problem for particles whose trajectories pass through a fixed grid at the end of each timestep, rather than recording the full history of individual particles. They are therefore unconditionally stable. Two steps are usually required to implement SL schemes: trajectory tracing and interpolation back to the grid. In this study, a backward in time SL scheme is used for the trajectory tracing, and the quasi-monotone scheme developed by Bermejo and Staniforth (1992) for the interpolation.

2.4.1 Trajectory tracing

The advantage of backward in time SL schemes is that the interpolant is defined from the Eulerian grid. In the case of a rectilinear grid, this reduces the complexity of the implementation and the numerical cost of the interpolation function. From a particle point of view, the goal is to find the starting points at the previous timestep for each grid point. Using Eq. (5) for 1 element and in 1D, the following equation has to be solved:

$$\frac{dx}{dt} = v_{\mathrm{f}}(x,t). \tag{14}$$

Knowing $x(t_{n+1}) = x_i$ ~~with i a grid point~~, $x(t_n) = x_d$ ~~with~~ d a departure point needs to be found.

In practice, the velocity field varies greatly in time and in space between each time-step, especially for porosity waves, so it is not easy to determine x_d. A common approach to overcome this limit is to use the mid-point scheme (Robert (1981)):

$$\frac{x_i - x_d}{\Delta t} = v_{\mathrm{f}}\left(\frac{x_i + x_d}{2}, t_{n+\frac{1}{2}}\right). \tag{15}$$

https://doi.org/10.5194/gmd-2023-189
Preprint. Discussion started: 24 October 2023
© Author(s) 2023. CC BY 4.0 License.

Geoscientific Model Development Discussions

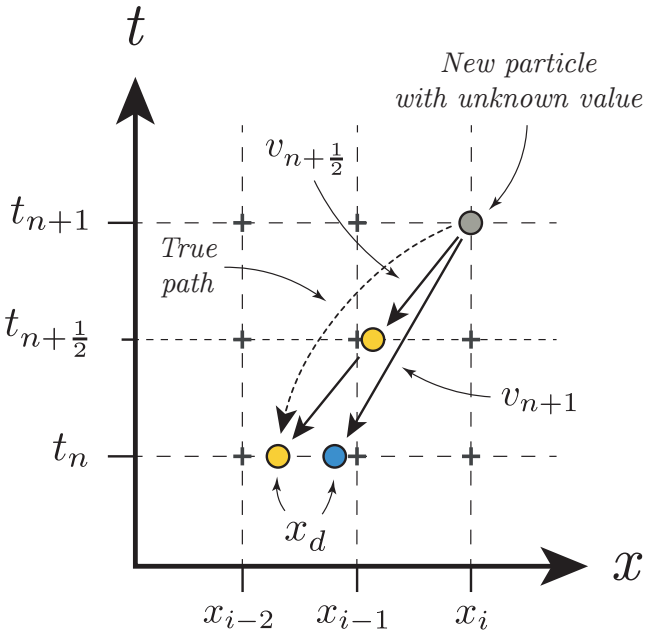

Figure 3. Summary of trajectory tracing for backward semi-Lagrangian schemes. The aim is to find the value of the advected quantity at the position x_i and at the timestep t_{n+1}. The blue particle uses the velocity at $n+1$. The yellow particle shows the midpoint method, using an approximation of the velocity at $n+\frac{1}{2}$. The value of the particle at position x_d can then be interpolated at t_n to obtain the value at x_i at t_{n+1}.

The assumption behind the mid-point rule is that the velocity remains constant at the mid-point value during each timestep. This ensures that each trajectory is linear, with the mid-point being the average of the positions of its endpoints (Fig. 3). This method is a second-order accurate trajectory method in both space and time.

Equation (15) must be solved implicitly, because x_d is present on both sides of the equation, and therefore requires iterations. It can be achieved for r iterations in that form:

$$x_d^{r+1} = x_i - \Delta t v_{\mathrm{f}} \left(\frac{x_i + x_d^r}{2}, t_{n+\frac{1}{2}} \right). \tag{16}$$

This also requires interpolation of v_{f} at $t_{n+\frac{1}{2}}$ r times. A minimum of 3 iterations while using linear interpolation has been shown to be sufficient in most cases (e.g., McDonald, 1984).

https://doi.org/10.5194/gmd-2023-189
Preprint. Discussion started: 24 October 2023
© Author(s) 2023. CC BY 4.0 License.

Geoscientific Model Development Discussions

2.4.2 Interpolation

In most cases, x_d does not correspond to a stencil point on the grid (see Fig. 3). In this case, interpolation is required to retrieve the value of the unknown at x_d:

$$C(x_d,t) = \mathcal{L}\left[C(x_{i_k}),t\right], \tag{17}$$

where $\mathcal{L}$ is an interpolation operator and x_{i_k} represents the nodes of the cell containing x_d.

Commonly, cubic interpolants are ~~applied~~ as ~~it is~~ a good compromise between performance and accuracy (e.g., Chandrasekar, 2022). The Godunov's theorem still applies to linear SL schemes and since cubic interpolation is third-order in space, it introduces oscillations and overshoots for high gradients. To overcome this limitation, quasi-monotone (QM) SL schemes were developed by Bermejo and Staniforth (1992). The term QM means that the scalar field values cannot exceed the range of the previous timestep, but can still develop wiggles inside that range. Quasi-monotonicity is equivalent to the notion of essentially non-oscillatory (Bermejo, 2001). A disadvantage of this method is an increased numerical diffusion, especially for high Courant number. A maximum Courant number of 1.5 is generally used (e.g., Smith, 2000).

To implement QMSL schemes, let's define C^- and C^+ as the minimum and maximum scalar values of the nodes of the cell containing x_d and C^H as the high order non-monotone interpolant. Then, a local ~~clipping~~ can be applied at the end of each timestep:

$$C^M(x_d,t) = \begin{cases} C^+(x_d,t) & \text{if} \quad C^H(x_d,t) > C^+(x_d,t) \\ C^-(x_d,t) & \text{if} \quad C^H(x_d,t) < C^-(x_d,t) \\ C^H(x_d,t) & \text{otherwise,} \end{cases} \tag{18}$$

where C^M is the quasi-monotone interpolant. Equation (18) can be rewritten in a more compact way:

$$C^M(x_d,t) = \min\left\{\max\left[C^-(x_d,t), C^H(x_d,t)\right], C^+(x_d,t)\right\}. \tag{19}$$

Formally, this formulation is equivalent to a linear combination between a high order interpolant and a first order (monotone) interpolant (Bermejo, 2001).

2.5 Marker-in-cell schemes

Marker-In-Cell (MIC) schemes share the same ambition as SL schemes, such as being unconditionally stable, but are closer to Lagrangian schemes. They record the complete history of individual particles, called markers and interpolate their values on a fixed grid. This approach has the advantage of reducing ~~greatly~~ numerical diffusion and making MIC schemes unconditionally stable. In addition to trajectory tracing and interpolation, the MIC schemes require markers to be generated within the domain of the model.

https://doi.org/10.5194/gmd-2023-189
Preprint. Discussion started: 24 October 2023
© Author(s) 2023. CC BY 4.0 License.

Geoscientific Model Development Discussions

2.5.1 Initial marker generation and reseeding of particles

The number of markers per cell required can vary depending on the complexity of the problem. Here, 5 markers per cell dimension, effectively 25 in 2D. This is generally sufficient to achieve good accuracy (e.g., Gerya, 2019). The initial value of each marker can then be obtained by linear interpolation from the initial conditions of the Eulerian grid.

For highly divergent flows, it is necessary to regenerate or remove markers during the simulation, as particles will accumulate in zones with negative divergence values and create a gap in zones with positive divergence values. For reseeding, a strategy similar to Keller et al. (2013) is used. If the marker density per cell is less than 25% of the initial density, new markers are generated and are assigned the value of the nearest marker. The old markers are discarded after this step. For marker accumulation, the marker density cannot exceed twice the initial density. If it does, a quarter of the markers are discarded at random.

2.5.2 Trajectory tracing

The goal of trajectory tracing for MIC schemes is to determine the position of each marker at the next timestep. The same equation as Eq. 14 is solved. However, compared to backward SL where the final position is known, the unknown in this case is the position of the arrival point. We can rewrite Eqs. 15 and 16 for the unknown x_a, the arrival point, using the mid-point rule as:

$$\frac{x_a - x_d}{\Delta t} = v_{\mathrm{f}}\left(\frac{x_a + x_d}{2}, t_{n+\frac{1}{2}}\right), \tag{20}$$

and

$$x_a^{r+1} = x_d + \Delta t v_{\mathrm{f}}\left(\frac{x_a + x_d^r}{2}, t_{n+\frac{1}{2}}\right). \tag{21}$$

As for the SL schemes, it is necessary to interpolate the velocity field r times.

Since classical interpolants do not retain the physical properties of the velocity field, such as its divergence, a simple bilinear interpolation may lead to unphysical clustering of markers on the time scale of a numerical model. To address this issue, Pusok et al. (2017) explored different interpolants and showed the advantages of using the so-called LinP interpolation scheme (Gerya, 2019). The LinP interpolation scheme is an empirical relationship that combines two linear interpolants defined at the sides and at the center of each cell. It is defined as:

$$v_{\mathrm{f}}\left(\frac{x_a + x_d}{2}, t_{n+\frac{1}{2}}\right) = A\mathcal{L}\left[v_{\mathrm{f}}\left(x_{\mathrm{side}}, t_{n+\frac{1}{2}}\right)\right] + (1-A)\mathcal{L}\left[v_{\mathrm{f}}\left(x_{\mathrm{center}}, t_{n+\frac{1}{2}}\right)\right], \tag{22}$$

with A, a constant commonly equal to $2/3$, $\mathcal{L}$ a linear interpolant, and x_{side} and x_{center} the position of the sides and center of the cell containing x_d.

https://doi.org/10.5194/gmd-2023-189
Preprint. Discussion started: 24 October 2023
© Author(s) 2023. CC BY 4.0 License.

Geoscientific Model Development Discussions
Open Access
EGU

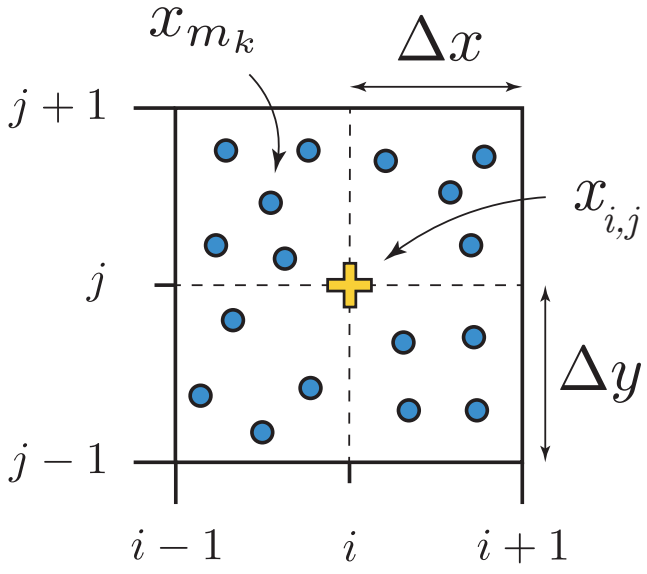

Figure 4. Sketch showing the geometric relationship in 2D between a point $x_{i,j}$ of the Eulerian grid and the markers x_{m_k} used for the interpolation on a regular grid. The value at the point $x_{i,j}$ is interpolated from the markers x_{m_k} contained inside the four neighbouring cells. $x_{i,j}$ is fixed in time and in space, whereas the position of the markers x_{m_k} are time-dependent.

2.5.3 Interpolation

After calculating the position of the markers, it is necessary to interpolate back on the Eulerian grid. This is more complex than for SL schemes because the markers are not uniformly distributed for a non-trivial velocity field. Therefore, even for regular Eulerian grid, interpolation is performed on an unstructured grid as it is based on the position of the markers.

In this case, interpolation is required to obtain the values of our unknown at x_i, ~~where i is a grid point:~~

$$C\left(x_i, t_{n+1}\right) = \mathcal{L}\left[C\left(x_{i_{m_k}}\right), t_{n+1}\right], \tag{23}$$

where $x_{i_{m_k}}$ represents the surrounding markers used for the interpolant and $\mathcal{L}$ is an interpolation operator. Typically, all markers found in the surrounding cells are used for the interpolation (e.g., Gerya and Yuen, 2003b). Linear interpolants are used because they prevent oscillations, and marker densities are high enough to prevent numerical diffusion. The relationship between the markers and the grid is summarised on Fig. 4 in 2D.

3 Numerical test

To test the four advection schemes, the rotation of a cylinder in 2D is performed. The domain is a square of size 1.0×1.0 with a constant spacing of $\Delta x = \Delta y = 0.005$ for a resolution of 201×201 nodes. The radius of the cylinder is $24\Delta x$, ~~contains~~ a

https://doi.org/10.5194/gmd-2023-189
Preprint. Discussion started: 24 October 2023
© Author(s) 2023. CC BY 4.0 License.

Geoscientific Model Development Discussions
Open Access
EGU

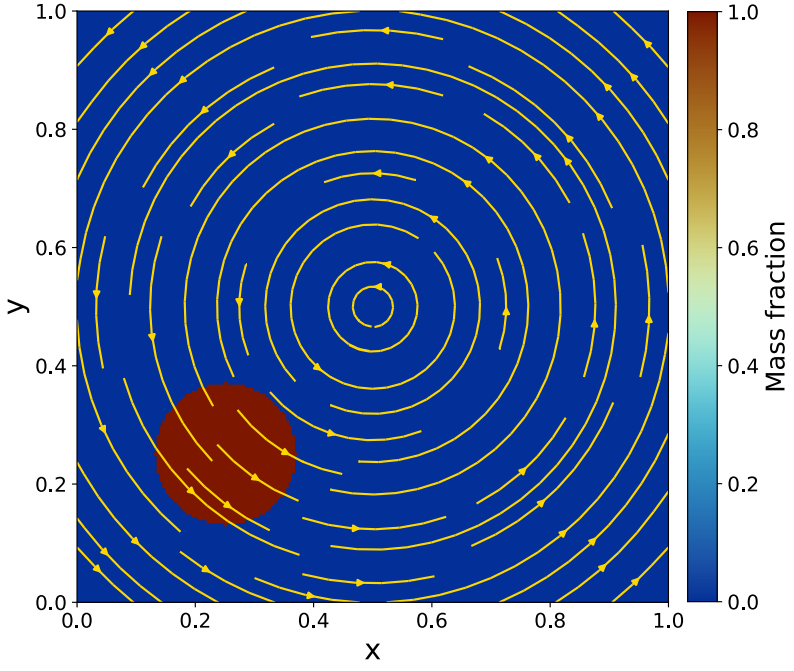

Figure 5. Initial conditions for the numerical test consisting of the rotation of a cylinder. The yellow arrows show the velocity field.

mass fraction of 1.0 and is centered at coordinates $(0.25;0.25)$. The initial conditions are shown ~~on~~ Fig. 5. The time increment ~~Δt is set to 400 s~~ with $\omega = \pi \times 10^{-5} s^{-1}$ so that it takes 500 timesteps to make a full revolution. The velocity is defined as $\boldsymbol{v} = (-\omega(y-0.5);\omega(x-0.5))$ so that the rotation is anti-clock wise and the centre of it is at coordinates $(0.5;0.5)$. The Courant numbers inside the cylinder range between 0.45 and 0.8. Results after 2 revolutions are shown ~~on~~ Fig. 6 for the four schemes.

To compare and quantify the results of the different schemes, 4 different quantities were monitored: the mass conservation (M), the total error (E_{tot}), the maximum value of the final mass fraction ($\max(C_{\text{f}})$) and the computational time of ~~1~~ timestep (t_{scheme}).

The mass conservation is defined as:

$$M = \frac{\sum_{k=1}^{K} \left(C_{\text{f}}^k S_k\right)}{\sum_{k=1}^{K} \left(C_0^k S_k\right)}, \tag{24}$$

where k is a 2D grid point index, K is the total number of grid points, C_{f}^k is the final mass fraction at the index k, C_0^k is the initial mass fraction at index k and S_k is the surface area of the cell at index k.

The total error of the scheme is defined as the mean square error:

$$E_{\text{tot}} = \frac{1}{K} \sum_{k=1}^{K} \left(C_0^k - C_{\text{f}}^k\right)^2. \tag{25}$$

https://doi.org/10.5194/gmd-2023-189
Preprint. Discussion started: 24 October 2023
© Author(s) 2023. CC BY 4.0 License.

Geoscientific Model Development Discussions

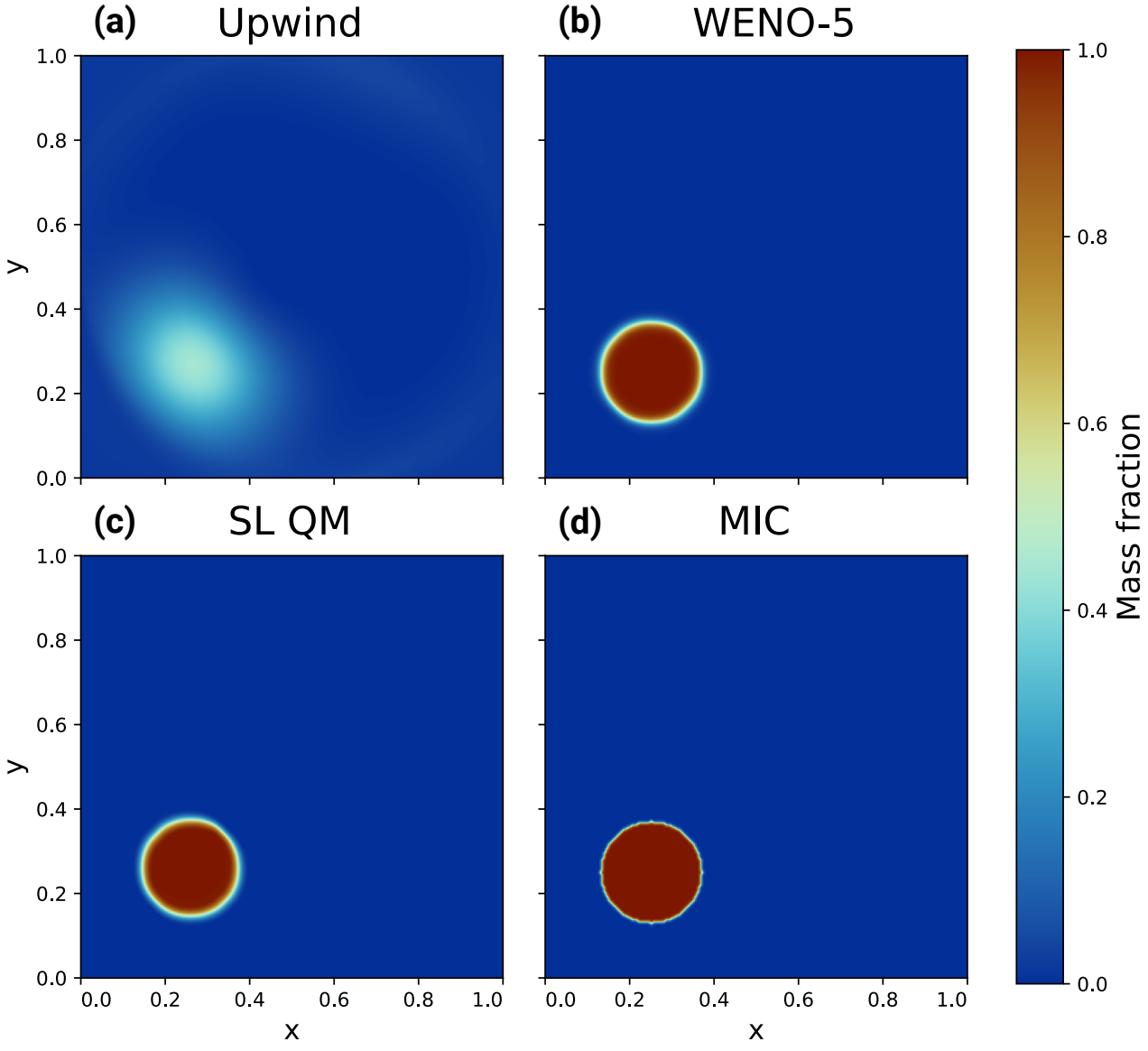

Figure 6. Results of the rotational test after two revolutions for the upwind, WENO-5, SL QM and MIC schemes (a)-(d). Note that the upwind scheme was run with $\Delta t = 80\,s$ due to stability issues.

https://doi.org/10.5194/gmd-2023-189
Preprint. Discussion started: 24 October 2023
© Author(s) 2023. CC BY 4.0 License.

Geoscientific Model Development Discussions
Open Access
EGU

Table 2. Results of the two numerical tests for four advection schemes.

Numerical schemes	M	E_{tot}	$\max(C)$	t_{scheme} (ms)
Upwind	1.000	31.00×10^{-3}	0.233	0.225
WENO-5	1.000	3.21×10^{-3}	1.001	9.856
SL QM	0.827	11.97×10^{-3}	1.000	224.450
MIC	1.000	0.68×10^{-3}	1.000	710.765

The results are reported in Table 2. This shows the strong numerical diffusion of the upwind scheme and its high E_{tot} due to its first order in time and space. WENO-5 shows no oscillation and a good accuracy, being fifth order in space and third in time. SL QM is not mass conservative for this problem but show a relatively good accuracy, being third order in space and second in time and is monotone. Finally, for this test, the MIC scheme is mass conservative, monotone and shows the best accuracy. This simple test highlights the properties of each scheme, but uses a velocity field that is divergence-free and without sharp variations. This is not the case for a real case problem. Coupling with a two-phase flow system is therefore necessary to assert which scheme is the more suitable in this case.

4 Coupling chemical advection and two-phase flow

Solving Eq. (5) for concrete cases implies having an expression for v_{f} at each timestep. In this section, Eq. (5) is coupled to a transport model based on two-phase flow formalism. This transport model is used to model magma ascent in a porous solid phase. The main mechanism of transport is decompaction weakening, buoyancy and failure, and combines the formulations of Connolly and Podladchikov (2007a) and Vasilyev et al. (1998). It considers a compressible visco-elastic matrix with incompressible solid grains and an incompressible fluid phase, and neglects the effect of shear stresses on fluid flow and compaction.

4.1 Two-phase Flow Formulation

In the case of a laminar fluid flow, conservation of momentum for the fluid can be expressed using Darcy's law:

$$\phi(\boldsymbol{v_{\text{f}}} - \boldsymbol{v_{\text{s}}}) = -\frac{k(\phi)}{\mu_{\text{f}}}(\nabla P_{\text{f}} + \rho_{\text{f}}\boldsymbol{g}), \tag{26}$$

with P_{f} the fluid pressure (in Pa), k the permeability (m^2), a function of the filled porosity ϕ, μ_{f} the fluid viscosity (Pa.s), and $\boldsymbol{g}$ the gravity vector (m.s^{-2}).

The relation between permeability and porosity is assumed to follow the Kozeny-Carman law (Carman, 1939; Costa, 2006):

$$k = a\phi^3, \tag{27}$$

where a is a proportionality constant.

https://doi.org/10.5194/gmd-2023-189
Preprint. Discussion started: 24 October 2023
© Author(s) 2023. CC BY 4.0 License.

Geoscientific Model Development Discussions

The effective pressure P_e is defined as the difference between lithostatic pressure and fluid pressure:

$$P_e = P_{\text{lith}} - P_{\text{f}}, \tag{28}$$

with P_{lith} the lithostatic pressure or the vertical load (in Pa). Substituting Eq. (28) in Eq. (26) and assuming constant rock density, we obtain:

$$\phi(\boldsymbol{v_f} - \boldsymbol{v_s}) = \frac{k(\phi)}{\mu_{\text{f}}} \left(\nabla P_e + \Delta\rho \boldsymbol{g}\right). \tag{29}$$

Considering the solid phase as a Maxwell body, we introduce rheology as the sum of viscous and poro-elastic deformation:

$$\nabla \cdot \boldsymbol{v_s} = -\frac{P_e}{\zeta(\phi, P_e)} - \phi^b \beta_\phi \frac{\partial P_e}{\partial t}, \tag{30}$$

where ζ is the volume viscosity of the rock (in Pa.s), b, a constant, and β_ϕ the pore compressibility modulus (Pa^{-1}). The terms on the right-hand side represent viscous and poro-elastic deformation, respectively. Equation (30) is valid on the basis that shear stress is neglected.

The volume viscosity ζ is defined as a function of ϕ and P_e:

$$\zeta = \frac{\mu_{\text{s}}}{\phi^m}[\frac{1}{R} - H(P_e)(\frac{1}{R} - 1)], \tag{31}$$

with μ_{s} the shear viscosity of the rock (in Pas), m a constant, and R the decompaction weakening factor, defined as the inverse of the R factor in Connolly and Podladchikov (2007a). $H(P_e)$ is originally defined as the Heaviside function but is here approximated by a hyperbolic tangent function as similarly done by Räss et al. (2018).

We approximate here β_ϕ as the inverse of G, the shear modulus of the rock (in Pa):

$$\beta_\phi \approx \frac{1}{G}. \tag{32}$$

This is valid for cylindrical pores, as described by Yarushina and Podladchikov (2015).

Summing up the right-hand sides of Eqs. (1) and (2) describing mass conservation and neglecting the change of densities, we obtain the total volumetric flux of material. Applying the divergence operator, we can derive:

$$\nabla \cdot [\boldsymbol{v_s} + \phi(\boldsymbol{v_f} - \boldsymbol{v_s})] = 0. \tag{33}$$

We can then substitute Eqs. (29) and (30) in Eq. (33) to obtain:

$$\frac{P_e}{\zeta(\phi, P_e)} + \frac{\phi^b}{G}\frac{\partial P_e}{\partial t} = \nabla \cdot \left[\frac{k(\phi)}{\mu_{\text{f}}} \left(\nabla P_e + \Delta\rho \boldsymbol{g}\right)\right]. \tag{34}$$

https://doi.org/10.5194/gmd-2023-189
Preprint. Discussion started: 24 October 2023
© Author(s) 2023. CC BY 4.0 License.

Geoscientific Model Development Discussions
Open Access
EGU

315 In addition, developing Eq. (1) with the assumption that ϕ is much smaller than unity, and substituting with Eq. (30) yields:

$$\frac{\partial \phi}{\partial t} = -\frac{P_e}{\zeta(\phi, P_e)} - \frac{\phi^b}{G}\frac{\partial P_e}{\partial t}. \tag{35}$$

Equation (34) can be seen as the mass conservation equation of the system, relating the flux densities of the solid and fluid phases. Equation (35) relates the evolution of porosity with the deformation of the solid phase.

Solving these two coupled equations for P_e and ϕ allows the calculation of $\boldsymbol{v_s}$ and $\boldsymbol{v_f}$ from Eqs. (30) and (29) at each
320 timestep, making the link with Eq. (5).

4.2 Nondimensionalization and numerical approach

To mitigate numerical errors, a dimensionless scaling of the system is applied. We define the following scaling variables (McKenzie, 1984; Connolly and Podladchikov, 1998):
the characteristic porosity ϕ^*:

325 $$\phi^* = \phi_0, \tag{36}$$

with ϕ_0, the background porosity.

The characteristic viscous compaction length L^*:

$$L^* = \sqrt{\frac{\mu_s k_0}{\phi_0 \mu_{f0}}}, \tag{37}$$

with k_0, the background permeability (in m^2).
330 The characteristic effective pressure P_e^*:

$$P_e^* = L^* \Delta\rho g. \tag{38}$$

The characteristic fluid flux q_f^*:

$$q_f^* = \frac{\mu_{f0}}{\phi_0}\Delta\rho g L^*. \tag{39}$$

The characteristic time t^*:

335 $$t^* = \frac{L^*}{\sqrt{q_f^*}}. \tag{40}$$

https://doi.org/10.5194/gmd-2023-189
Preprint. Discussion started: 24 October 2023
© Author(s) 2023. CC BY 4.0 License.

Geoscientific Model Development Discussions

De, the Deborah number:

$$De = \beta_\phi P_e^*. \tag{41}$$

De is formally the ratio of the relaxation time to the observation time (Reiner, 1964), and here characterises the ratio between viscous and elastic deformation.

Using these variables with Eqs. (29), (30), (34) and (35), and rearranging, we obtain the dimensionless system of equations:

$$\frac{\partial p}{\partial t} = \frac{1}{\varphi^b De} \times \left(\nabla \cdot \left[\varphi^n \left(\nabla p + 1 \right) \right] - \frac{\varphi p}{\frac{1}{R} - H(p)\left(\frac{1}{R} - 1\right)} \right), \tag{42}$$

$$\frac{\partial \varphi}{\partial t} = - \left[\frac{\varphi p}{\frac{1}{R} - H(p)\left(\frac{1}{R} - 1\right)} + \varphi^b De \frac{\partial p}{\partial t} \right], \tag{43}$$

$$\nabla \cdot \boldsymbol{u_s} = \frac{\partial \varphi}{\partial t}, \tag{44}$$

$$\boldsymbol{u_f} = \varphi^{n-1} \left(\nabla p + 1 \right) + \boldsymbol{u_s}, \tag{45}$$

where φ, p, $\boldsymbol{u_s}$ and $\boldsymbol{u_f}$ are the dimensionless porosity, the dimensionless effective pressure, the dimensionless solid velocity and the dimensionless fluid velocity, respectively.

Equations (42) and (43) are strongly coupled and highly stiff due to the nonlinearity of the system and require an efficient numerical solver. DifferentialEquations.jl (Rackauckas and Nie, 2017), a robust ordinary differential equation (ODE) solver, was used. This ~~method~~ has the advantage of simplicity, both in concept and in coding, and allows arbitrary orders of accuracy in time to be easily tested using different ODE solvers.

Equations (42) and (43) are first discretised in space using finite differences on a uniform Cartesian grid in 2D, and then integrated in time using the Trapezoidal Rule with the second order Backward Difference Formula (TR-BDF2) scheme, an implicit scheme suitable for highly stiff problems (Bank et al., 1985). It uses adaptive time-stepping and Newton method as a non-linear solver, using automatic differentiation to compute the Jacobian matrix. Knowing φ and p, Eqs. (44) and (45) are then solved to compute $\boldsymbol{u_s}$ and $\boldsymbol{u_f}$ at each timestep. The boundary conditions are periodic in all directions for all models. The system is then dimensionalised back.

https://doi.org/10.5194/gmd-2023-189
Preprint. Discussion started: 24 October 2023
© Author(s) 2023. CC BY 4.0 License.

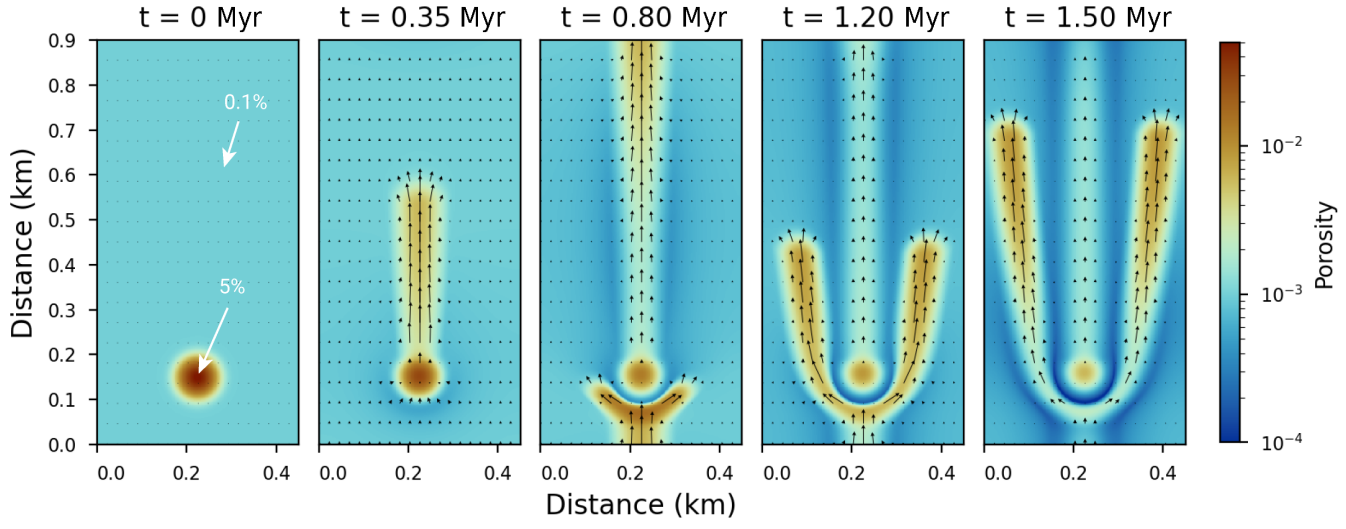

Figure 7. Reference evolution of the porosity in a 2D model from an initial Gaussian anomaly, which forms porosity waves. The superimposed vector field shows the melt velocity. Periodic boundaries are applied on all sides. The initial porosity anomaly is a Gaussian function with a maximum value of 5%. The background porosity is 0.1%. The spatial resolution of the grid is 300×600. The physical parameters used are listed in Table 3. The melt velocity is scaled by relative magnitude.

4.3 Application to magmatic system

To assert the behaviour of the four advection schemes coupled with a two-phase flow system, we model the ascent of a magmatic anomaly. The spatial domain is a 2D regular grid of 450 by 900 m and the total physical time is 1.5 Ma. The initial melt fraction distribution is defined using the following 2D Gaussian function:

$$\phi = \phi_0 + \phi_{max} \times \exp\left(-\frac{(x-x_0)^2 + (z-z_0)^2}{\sigma^2}\right), \tag{46}$$

with ϕ_0, the background porosity defined as 0.1%, ϕ_{max}, the maximum porosity defined as 5%, and x_0 and z_0, the center of the anomaly. σ is the standard deviation of the Gaussian and is 30. All physical parameters and corresponding scaling variables used are reported in Table 3. The evolution of porosity is shown on Fig. 7. All models were performed on a single computer with an Intel Xeon Gold 6128 processor and 128 GB of RAM.

The melt fraction is linked with two different arbitrary chemical compositions: a basaltic composition for the background melt fraction and an andesitic composition for the anomaly. The goal is not to model a realistic magmatic system, but to investigate how the advection schemes can numerically affect the predictions of the model. The two compositions are reported in Table 4. No feedback between the melt compositions and the physical properties of the melt were considered, to prevent the advection schemes to influence on the two-phase flow. In nature, the melt composition has an effect on the melt viscosity and density. The maximum timestep allowed for the two-phase flow is constrained by the Courant number associated with the

https://doi.org/10.5194/gmd-2023-189
Preprint. Discussion started: 24 October 2023
© Author(s) 2023. CC BY 4.0 License.

Geoscientific Model Development Discussions
Open Access
EGU

Table 3. Parameters and corresponding scaling variables used in the models.

Parameter	Symbol	Value	Unit
Melt viscosity	μ_f	100	Pa.s
Rock shear viscosity	μ_s	10^{19}	Pa.s
Density contrast between solid and melt	$\Delta\rho$	500	$kg.m^{-3}$
Weakening parameter	R	100	
Shear modulus	G	3.5×10^{19}	Pa
Background porosity	ϕ_0	10^{-3}	
Exponent for bulk viscosity term	m	1	
Exponent for poro-elastic term	b	1	
Permeability constant	a	10^{-7}	
Gravity acceleration	g	9.81	$m.s^{-2}$
Characteristic viscous compaction length	L^*	100	m
Characteristic effective pressure	P_e^*	490332.5	Pa
Characteristic time	t^*	0.65	Myr
Characteristic fluid flux	q_f^*	4.9×10^{-12}	$m.s^{-1}$
Deborah Number	De	1.4×10^{-5}	

Table 4. Melt compositions in wt% used in the models. 1: Recalculated from Giordano and Dingwell (2003). 2: Recalculated from Neuville et al. (1993).

Oxide (wt%)	Basalt[1]	Andesite[2]
SiO_2	48.32	59.87
TiO_2	1.65	0.82
Al_2O_3	16.72	16.93
FeO(T)	10.41	5.28
MgO	5.31	3.28
CaO	10.75	5.70
Na_2O	3.85	3.76
K_2O	1.99	1.36
H_2O	1.00	3.00

melt velocity. Its maximum value allowed for upwind and WENO-5 is 0.7 but 1.5 for QMSL and MIC to take advantage of the extended stability of these schemes. The results for the evolution of the silica content in the melt are shown on Fig. 8.

As there is no analytical solution to this particular problem, it is not possible to directly calculate the numerical error of the different advection schemes. Nevertheless, we can compute the mass conservation of the advected quantities. The total mass of the melt composition is conserved, as it is renormalized to 100% at each timestep. However, it is not necessary the case for

https://doi.org/10.5194/gmd-2023-189
Preprint. Discussion started: 24 October 2023
© Author(s) 2023. CC BY 4.0 License.

Geoscientific Model Development
Discussions

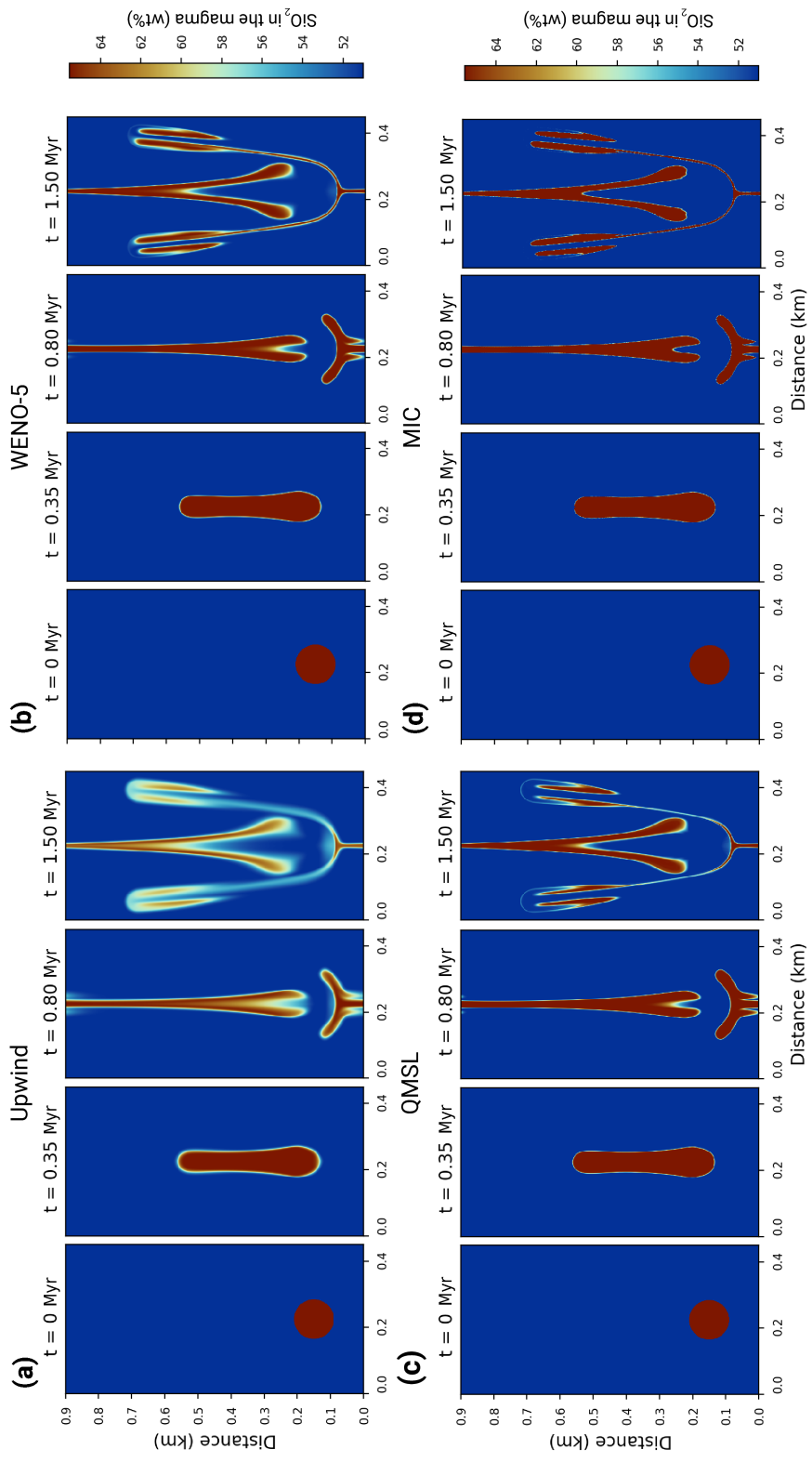

Figure 8. Evolution of the silica content in the melt for four different advection schemes: upwind, WENO-5, QMSL and MIC (a)-(d). The Gaussian anomaly of porosity is associated with an andesitic composition, whereas the background porosity has a basaltic composition. The corresponding two-phase flow has an adaptive timestep limited to a maximum value of Courant number below 0.7 for the upwind and WENO-5 schemes and below 1.5 for QMSL and MIC. The spatial resolution is 300×600 nodes. The physical parameters used for the two-phase flow are reported in Table 3 and are identical for all models.

https://doi.org/10.5194/gmd-2023-189
Preprint. Discussion started: 24 October 2023
© Author(s) 2023. CC BY 4.0 License.

Geoscientific Model Development Discussions
Open Access
EGU

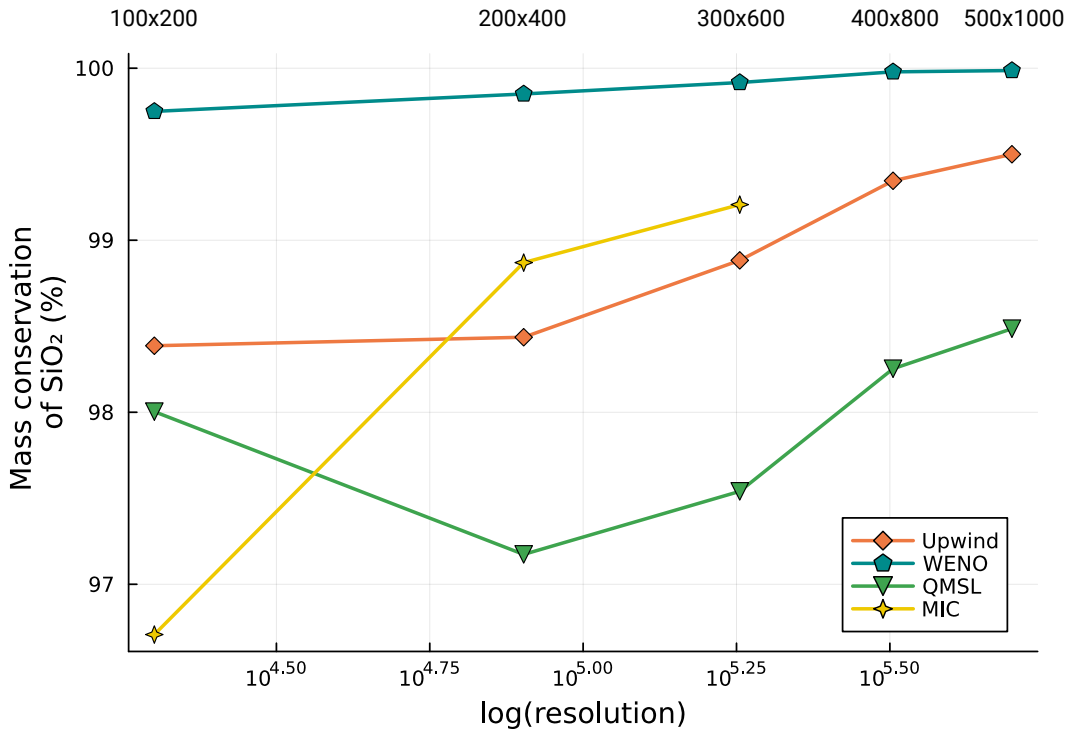

Figure 9. Mass conservation of silica content in the melt fraction for four different advection schemes and five different spatial resolutions. The Courant number used is 0.7 for WENO-5 and upwind and 1.5 for QMSL and MIC. The resolutions are 100×200, 200×400, 300×600, 400×800 and 500×1000. MIC models for 400×800 and 500×1000 were not performed due to RAM memory saturation. The physical parameters used are reported in Table 3.

each individual oxide. In that light, similar to Eq. (24), we monitor the mass conservation of SiO_2 (M_{SiO_2}) in the melt at each timestep:

$$M_{SiO_2} = \frac{\sum_{k=1}^{K} \left(\phi^k C^k_{SiO_2} S_k\right)}{\sum_{k=1}^{K} \left(\phi^k_0 C^k_{SiO_{2_0}} S_k\right)}, \tag{47}$$

where ϕ^k and ϕ^k_0 are the current and initial porosity at index k, and $C^k_{SiO_2}$ and $C^k_{SiO_{2_0}}$ the current and initial SiO_2 composition in the melt at the index k.

The melt fraction ϕ is conserved through the models, as Eqs. (42) and (43) are solved using a conservative discretisation. Therefore, M_{SiO_2} only monitors the effects of the advection schemes. To quantify how the mass conservation evolves, the same model was performed at five different resolutions: 100×200, 200×400, 300×600, 400×800 and 500×1000. The values of M_{SiO_2} for each resolution are shown on Fig. 9. The running time of each model is reported on Fig. 10.

https://doi.org/10.5194/gmd-2023-189
Preprint. Discussion started: 24 October 2023
© Author(s) 2023. CC BY 4.0 License.

Geoscientific Model Development Discussions
Open Access
EGU

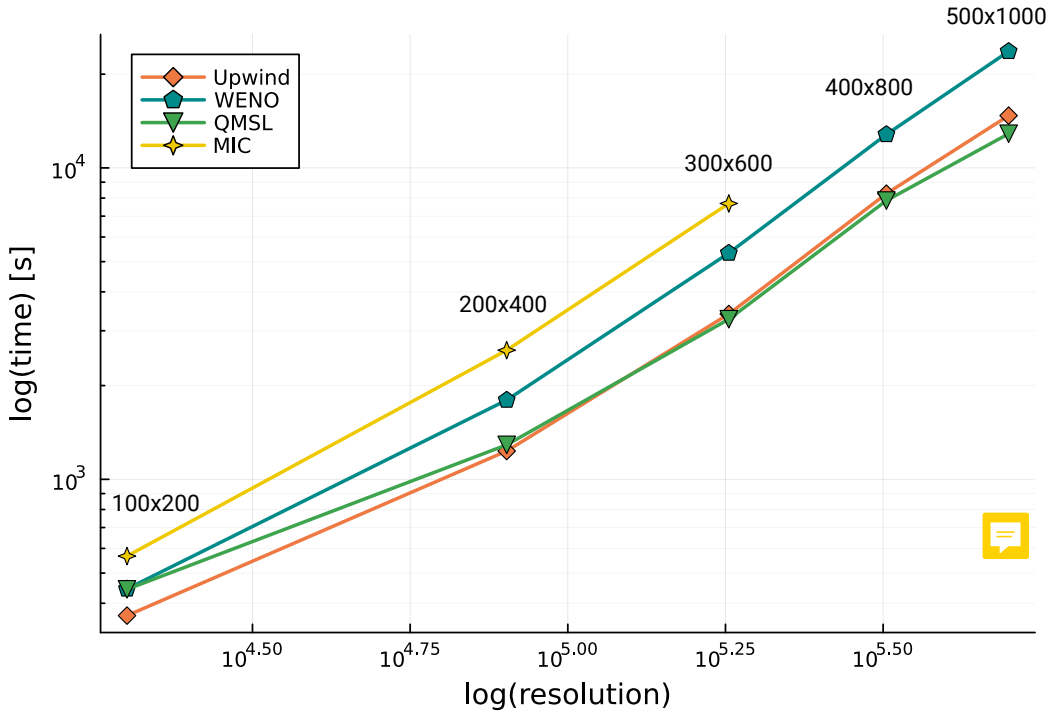

Figure 10. Total running time of two-phase flow system coupled with four different advection schemes and five different resolutions. The Courant number used is 0.7 for WENO-5 and upwind and 1.5 for QMSL and MIC. The resolutions are 100×200, 200×400, 300×600, 400×800 and 500×1000. MIC models for 400×800 and 500×1000 were not performed due to RAM memory saturation. The physical parameters used are reported in Table 3.

5 Results and discussion

The numerical models produced allow a better understanding of the process of passive chemical transport in magma within porosity waves and the impact of each advection scheme on the magma composition over time. All models confirm two distinct composition domains at the top of the porosity waves at the end of the simulations (Fig. 8). It is effectively a mixture of the compositions from the initial background porosity and from the anomaly. This is due to melt being incorporated by the waves as they rise, and has also been reported in previous studies (e.g., Jordan et al., 2018).

Comparing the results of the four algorithms, it is clear that the upwind scheme has the highest amount of numerical diffusion and the lowest accuracy, which increases chemical mixing for non-physical reasons. WENO-5 and QMSL exhibit similar results in terms of numerical diffusion while MIC shows the lowest amount with almost purely advective behaviour (Fig. 8). This is consistent with the numerical tests (Fig. 6). In terms of mass conservation, the silica content is not conserved in all four schemes (Fig. 9). WENO-5 gives the best results, with a mass conservation ranging from 99.75 to 99.99% from the lowest to the highest resolution. MIC and upwind show values around 98.5 to 99.5% at medium resolution, and QMSL

https://doi.org/10.5194/gmd-2023-189
Preprint. Discussion started: 24 October 2023
© Author(s) 2023. CC BY 4.0 License.

Geoscientific Model Development Discussions

exhibits significantly lower values, ranging from 97.17 to 98.49%. Concerning performance, two factors affect the results: the stability of the advection schemes, that is linked on how often the two-phase flow solver is called, and the performance of the advection schemes themselves (Fig. 10). QMSL shows the best scaling as it has both an extended stability domain and a low computational cost. upwind shows similar performance despite being bounded by the Courant condition. ~~This is due to its very simple algorithm~~. WENO-5 has a higher computational cost, up to twice that of QMSL and upwind at high resolution. Finally, MIC is the most computationally expensive, both in terms of memory and running time, although it has an extended stability domain. All the calculations were performed on a single core and the code could be further optimised, but this provides an idea of the cost of each method. For large-scale computations, the extended stability domain may be the dominant criterion for efficient computation, as all the advection schemes are explicit, don't require iterations and are easily parallelizable. The two-phase flow solver will then be the limiting factor in computational efficiency.

The upwind scheme is considered inadequate for this problem because of its high numerical diffusion and low accuracy. The MIC scheme shows very good results in terms of accuracy with the least amount of numerical diffusion and has no stability condition. However, it lacks mass conservation and is expensive in terms of computation and memory, since it needs to keep track on the markers. As the velocity field $\boldsymbol{v_f}$ is strongly divergent, it requires to frequently regenerate and delete markers, which adds complexity to the implementation and additional numerical cost. As a result, we consider this scheme to be too costly for this particular problem. In addition, the QMSL scheme shows very good performance with its extended stability field and good accuracy, but has very poor mass conservation. Attempts have been made to make SL schemes mass conservative, either globally (e.g., Bermejo and Conde, 2002; Zerroukat et al., 2002) or locally (e.g., Qiu and Shu, 2011). These methods require the conservative form of the advection equation, a global correction term or are only applicable to divergent free vector fields. The QMSL scheme could be a good candidate for problems where mass conservation is not critical, such as advection of solid properties or solving the advection part of the heat equation, still in the context of two-phase flow problems but is not suitable for chemical advection where mass conservation is important.

Based on these results, the WENO-5 advection scheme appears to perform best for this problem. Mass conservation is a critical property for studying mass balance and mass transport problems linked to magma transport at different scales on Earth and this algorithm obtains the best results. It also has good accuracy, reasonable performance and is easy to extend to higher dimensions. If complex boundary conditions are required, it is possible to reduce the 5 point spatial stencil to a 3 point stencil and simplify the implementation of the boundary conditions, using the Compact-Reconstruction WENO-5 (CRWENO-5) scheme (Ghosh and Baeder, 2012). This approach uses implicit candidate stencils, which makes parallel computing more difficult but not impossible (Ghosh et al., 2015).

6 Conclusions

In this study, a series of test was performed to determine which advection schemes is the most suitable for modelling chemical transport of a magma, we compared four of the most commonly used in the literature: the upwind, WENO-5, MIC, and QMSL

https://doi.org/10.5194/gmd-2023-189
Preprint. Discussion started: 24 October 2023
© Author(s) 2023. CC BY 4.0 License.

Geoscientific Model Development Discussions

schemes. To test them, we combined a 2D two-phase flow model, which describes the evolution of the melt fraction of a magma over time, with the chemical advection of its composition.

All algorithms, except the upwind scheme, are able to predict the melt composition with reasonable accuracy. However, mass conservation of each individual oxide in the melt is not fully achieved. Nevertheless, WENO-5 has the lowest amount of mass loss, even at low resolution, is explicit, easy to implement and to extend in 3D, although it is bound by the CFL condition. On the basis of these results, the WENO-5 scheme is the most appropriate to use for transporting magma composition during magma ascent. This is also valid for problems using similar formulations, such as chemical advection in aqueous fluids, and makes WENO-5 a suitable scheme for modelling reactive transport.

Code availability. The last version of the code used in this study allowing reproducibility of the data is available on GitHub at (https://github.com/neoscalc/ChemicalAdvectionPorosityWave.jl). Past and future versions are available at a permanent DOI repository (Zenodo) at: https://doi.org/10.5281/zenodo.8411354. The code is written in the Julia programming language. Refer to the repository's README for additional information. The code is distributed under the GPL-3.0 license.

Author contributions. HD and PL conceptualised the project. PL acquired the funding. HD conducted the study with input from NR. HD wrote the code and the original manuscript. NR and PL revised and edited the manuscript. All authors contributed to the discussions and interpretation of the results.

Competing interests. The contact author has declared that none of the authors have competing interests.

Acknowledgements. Funding was provided by the European Research Council (ERC) under the European Union's Horizon 2020 research and innovation programme (grant agreement No 850530).

https://doi.org/10.5194/gmd-2023-189
Preprint. Discussion started: 24 October 2023
© Author(s) 2023. CC BY 4.0 License.

References

Aharonov, E., Whitehead, J. A., Kelemen, P. B., and Spiegelman, M.: Channeling Instability of Upwelling Melt in the Mantle, Journal of Geophysical Research: Solid Earth, 100, 20 433–20 450, https://doi.org/10.1029/95JB01307, 1995a.

Aharonov, E., Whitehead, J. A., Kelemen, P. B., and Spiegelman, M.: Channeling Instability of Upwelling Melt in the Mantle, Journal of Geophysical Research: Solid Earth, 100, 20 433–20 450, https://doi.org/10.1029/95JB01307, 1995b.

Aharonov, E., Spiegelman, M., and Kelemen, P.: Three-Dimensional Flow and Reaction in Porous Media: Implications for the Earth's Mantle and Sedimentary Basins, Journal of Geophysical Research: Solid Earth, 102, 14 821–14 833, https://doi.org/10.1029/97JB00996, 1997.

Bank, R., Coughran, W., Fichtner, W., Grosse, E., Rose, D., and Smith, R.: Transient Simulation of Silicon Devices and Circuits, IEEE Transactions on Computer-Aided Design of Integrated Circuits and Systems, 4, 436–451, https://doi.org/10.1109/TCAD.1985.1270142, 1985.

Barcilon, V. and Lovera, O. M.: Solitary Waves in Magma Dynamics, Journal of Fluid Mechanics, 204, 121, https://doi.org/10.1017/S0022112089001680, 1989.

Bercovici, D., Ricard, Y., and Schubert, G.: A Two-Phase Model for Compaction and Damage: 1. General Theory, Journal of Geophysical Research: Solid Earth, 106, 8887–8906, https://doi.org/10.1029/2000JB900430, 2001.

Bermejo, R.: Analysis of a Class of Quasi-Monotone and Conservative Semi-Lagrangian Advection Schemes:, Numerische Mathematik, 87, 597–623, https://doi.org/10.1007/PL00005425, 2001.

Bermejo, R. and Conde, J.: A Conservative Quasi-Monotone Semi-Lagrangian Scheme, MONTHLY WEATHER REVIEW, 130, 8, 2002.

Bermejo, R. and Staniforth, A.: The Conversion of Semi-Lagrangian Advection Schemes to Quasi-Monotone Schemes, Monthly Weather Review, 120, 2622–2632, https://doi.org/10.1175/1520-0493(1992)120<2622:TCOSLA>2.0.CO;2, 1992.

Bessat, A., Pilet, S., Podladchikov, Y. Y., and Schmalholz, S. M.: Melt Migration and Chemical Differentiation by Reactive Porosity Waves, Geochemistry, Geophysics, Geosystems, 23, https://doi.org/10.1029/2021GC009963, 2022.

Bouilhol, P., Connolly, J. A., and Burg, J.-P.: Geological Evidence and Modeling of Melt Migration by Porosity Waves in the Sub-Arc Mantle of Kohistan (Pakistan), Geology, 39, 1091–1094, https://doi.org/10.1130/G32219.1, 2011.

Brown, M.: Granite: From Genesis to Emplacement, Geological Society of America Bulletin, 125, 1079–1113, https://doi.org/10.1130/B30877.1, 2013.

Carman, P. C.: Permeability of Saturated Sands, Soils and Clays, The Journal of Agricultural Science, 29, 262–273, https://doi.org/10.1017/S0021859600051789, 1939.

Chandrasekar, A.: Numerical Methods for Atmospheric and Oceanic Sciences, Cambridge University Press, 1 edn., https://doi.org/10.1017/9781009119238, 2022.

Clemens, J. D., Bryan, S. E., Mayne, M. J., Stevens, G., and Petford, N.: How Are Silicic Volcanic and Plutonic Systems Related? Part 1: A Review of Geological and Geophysical Observations, and Insights from Igneous Rock Chemistry, Earth-Science Reviews, 235, 104 249, https://doi.org/10.1016/j.earscirev.2022.104249, 2022.

Connolly, J. A. D. and Podladchikov, Y. Y.: Decompaction Weakening and Channeling Instability in Ductile Porous Media: Implications for Asthenospheric Melt Segregation, Journal of Geophysical Research, 112, B10 205, https://doi.org/10.1029/2005JB004213, 2007a.

Connolly, J. A. D. and Podladchikov, Y. Y.: Decompaction Weakening and Channeling Instability in Ductile Porous Media: Implications for Asthenospheric Melt Segregation, Journal of Geophysical Research, 112, B10 205, https://doi.org/10.1029/2005JB004213, 2007b.

https://doi.org/10.5194/gmd-2023-189
Preprint. Discussion started: 24 October 2023
© Author(s) 2023. CC BY 4.0 License.

Connolly, J. A. D. and Podladchikov, Yu. Yu.: Compaction-Driven Fluid Flow in Viscoelastic Rock, Geodinamica Acta, 11, 55–84, https://doi.org/10.1080/09853111.1998.11105311, 1998.

Costa, A.: Permeability-Porosity Relationship: A Reexamination of the Kozeny-Carman Equation Based on a Fractal Pore-Space Geometry Assumption, Geophysical Research Letters, 33, L02 318, https://doi.org/10.1029/2005GL025134, 2006.

Courant, R., Isaacson, E., and Rees, M.: On the Solution of Nonlinear Hyperbolic Differential Equations by Finite Differences, Communications on Pure and Applied Mathematics, 5, 243–255, https://doi.org/10.1002/cpa.3160050303, 1952.

Duretz, T., May, D. A., Gerya, T. V., and Tackley, P. J.: Discretization Errors and Free Surface Stabilization in the Finite Difference and Marker-in-Cell Method for Applied Geodynamics: A Numerical Study: FD-MIC SCHEME DISCRETIZATION ERRORS, Geochemistry, Geophysics, Geosystems, 12, n/a–n/a, https://doi.org/10.1029/2011GC003567, 2011.

Gerya, T. V.: Introduction to Numerical Geodynamic Modelling, Cambridge University Press, 2 edn., https://doi.org/10.1017/9781316534243, 2019.

Gerya, T. V. and Yuen, D. A.: Characteristics-Based Marker-in-Cell Method with Conservative Finite-Differences Schemes for Modeling Geological Flows with Strongly Variable Transport Properties, Physics of the Earth and Planetary Interiors, 140, 293–318, https://doi.org/10.1016/j.pepi.2003.09.006, 2003a.

Gerya, T. V. and Yuen, D. A.: Characteristics-Based Marker-in-Cell Method with Conservative Finite-Differences Schemes for Modeling Geological Flows with Strongly Variable Transport Properties, Physics of the Earth and Planetary Interiors, 140, 293–318, https://doi.org/10.1016/j.pepi.2003.09.006, 2003b.

Ghosh, D. and Baeder, J. D.: Compact Reconstruction Schemes with Weighted ENO Limiting for Hyperbolic Conservation Laws, SIAM Journal on Scientific Computing, 34, A1678–A1706, https://doi.org/10.1137/110857659, 2012.

Ghosh, D., Constantinescu, E. M., and Brown, J.: Efficient Implementation of Nonlinear Compact Schemes on Massively Parallel Platforms, SIAM Journal on Scientific Computing, 37, C354–C383, https://doi.org/10.1137/140989261, 2015.

Giordano, D. and Dingwell, D. B.: Non-Arrhenian Multicomponent Melt Viscosity: A Model, Earth and Planetary Science Letters, 208, 337–349, https://doi.org/10.1016/S0012-821X(03)00042-6, 2003.

Godunov, S. K. and Bohachevsky, I.: Finite Difference Method for Numerical Computation of Discontinuous Solutions of the Equations of Fluid Dynamics, Matematičeskij sbornik, 47(89), 271–306, 1959.

Gottlieb, S., Shu, C.-W., and Tadmor, E.: Strong Stability-Preserving High-Order Time Discretization Methods, SIAM Review, 43, 89–112, https://doi.org/10.1137/S003614450036757X, 2001.

Grasso, F. and Pirozzoli, S.: Shock-Wave-Vortex Interactions: Shock and Vortex Deformations, and Sound Production, Theoretical and Computational Fluid Dynamics, 13, 421–456, https://doi.org/10.1007/s001620050121, 2000.

Harlow, F. H., Evans, M., and Richtmyer, R. D.: A Machine Calculation Method for Hydrodynamic Problems, Los Alamos Scientific Laboratory of the University of California, 1955.

Harten, A., Engquist, B., Osher, S., and Chakravarthy, S. R.: Uniformly High Order Accurate Essentially Non-oscillatory Schemes, III, in: Upwind and High-Resolution Schemes, edited by Hussaini, M. Y., van Leer, B., and Van Rosendale, J., pp. 218–290, Springer, Berlin, Heidelberg, https://doi.org/10.1007/978-3-642-60543-7_12, 1987.

Hirsch, C.: Numerical Computation of Internal and External Flows: Fundamentals of Computational Fluid Dynamics, Elsevier/Butterworth-Heinemann, Oxford ; Burlington, MA, 2nd ed edn., 2007.

Jackson, M., Gallagher, K., Petford, N., and Cheadle, M.: Towards a Coupled Physical and Chemical Model for Tonalite–Trondhjemite–Granodiorite Magma Formation, Lithos, 79, 43–60, https://doi.org/10.1016/j.lithos.2004.05.004, 2005.

https://doi.org/10.5194/gmd-2023-189
Preprint. Discussion started: 24 October 2023
© Author(s) 2023. CC BY 4.0 License.

Jha, K., Parmentier, E. M., and Phipps Morgan, J.: The Role of Mantle-Depletion and Melt-Retention Buoyancy in Spreading-Center Segmentation, Earth and Planetary Science Letters, 125, 221–234, https://doi.org/10.1016/0012-821X(94)90217-8, 1994.

Jiang, G.-S. and Peng, D.: Weighted ENO Schemes for Hamilton–Jacobi Equations, SIAM Journal on Scientific Computing, 21, 2126–2143, https://doi.org/10.1137/S106482759732455X, 2000.

Jiang, G.-S. and Shu, C.-W.: Efficient Implementation of Weighted ENO Schemes, Journal of Computational Physics, 126, 202–228, https://doi.org/10.1006/jcph.1996.0130, 1996.

Johnson, T., Yakymchuk, C., and Brown, M.: Crustal Melting and Suprasolidus Phase Equilibria: From First Principles to the State-of-the-Art, Earth-Science Reviews, 221, 103 778, https://doi.org/10.1016/j.earscirev.2021.103778, 2021.

Jordan, J. S., Hesse, M. A., and Rudge, J. F.: On Mass Transport in Porosity Waves, Earth and Planetary Science Letters, 485, 65–78, https://doi.org/10.1016/j.epsl.2017.12.024, 2018.

Katz, R. F.: Magma Dynamics with the Enthalpy Method: Benchmark Solutions and Magmatic Focusing at Mid-ocean Ridges, Journal of Petrology, 49, 2099–2121, https://doi.org/10.1093/petrology/egn058, 2008.

Katz, R. F. and Weatherley, S. M.: Consequences of Mantle Heterogeneity for Melt Extraction at Mid-Ocean Ridges, Earth and Planetary Science Letters, 335–336, 226–237, https://doi.org/10.1016/j.epsl.2012.04.042, 2012.

Katz, R. F., Jones, D. W. R., Rudge, J. F., and Keller, T.: Physics of Melt Extraction from the Mantle: Speed and Style, Annual Review of Earth and Planetary Sciences, 50, 507–540, https://doi.org/10.1146/annurev-earth-032320-083704, 2022.

Kelemen, P. B., Hirth, G., Shimizu, N., Spiegelman, M., and Dick, H. J.: A Review of Melt Migration Processes in the Adiabatically Upwelling Mantle beneath Oceanic Spreading Ridges, Philosophical Transactions of the Royal Society of London. Series A: Mathematical, Physical and Engineering Sciences, 355, 283–318, 1997.

Keller, T.: Numerical Modeling of Magma Ascent and Emplacement in the Continental Lithosphere and Crust, Ph.D. thesis, ETH Zurich, https://doi.org/10.3929/ETHZ-A-010192539, 2013.

Keller, T. and Katz, R. F.: The Role of Volatiles in Reactive Melt Transport in the Asthenosphere, Journal of Petrology, 57, 1073–1108, https://doi.org/10.1093/petrology/egw030, 2016.

Keller, T., May, D. A., and Kaus, B. J. P.: Numerical Modelling of Magma Dynamics Coupled to Tectonic Deformation of Lithosphere and Crust, Geophysical Journal International, 195, 1406–1442, https://doi.org/10.1093/gji/ggt306, 2013.

LeVeque, R. J.: Numerical Methods for Conservation Laws, Lectures in Mathematics ETH Zürich, Birkhäuser Verlag, Basel ; Boston, 2nd ed edn., 1992.

LeVeque, R. J.: Finite Volume Methods for Hyperbolic Problems, Cambridge Texts in Applied Mathematics, Cambridge University Press, Cambridge, https://doi.org/10.1017/CBO9780511791253, 2002.

Liu, X.-D., Osher, S., and Chan, T.: Weighted Essentially Non-oscillatory Schemes, Journal of Computational Physics, 115, 200–212, https://doi.org/10.1006/jcph.1994.1187, 1994.

McDonald, A.: Accuracy of Multiply-Upstream, Semi-Lagrangian Advective Schemes, Monthly Weather Review, 112, 1267–1275, https://doi.org/10.1175/1520-0493(1984)112<1267:AOMUSL>2.0.CO;2, 1984.

McKenzie, D.: The Generation and Compaction of Partially Molten Rock, Journal of Petrology, 25, 713–765, https://doi.org/10.1093/petrology/25.3.713, 1984.

Neuville, D. R., Courtial, P., Dingwell, D. B., and Richet, P.: Thermodynamic and Rheological Properties of Rhyolite and Andesite Melts, Contributions to Mineralogy and Petrology, 113, 572–581, https://doi.org/10.1007/BF00698324, 1993.

https://doi.org/10.5194/gmd-2023-189
Preprint. Discussion started: 24 October 2023
© Author(s) 2023. CC BY 4.0 License.

Omlin, S., Malvoisin, B., and Podladchikov, Y. Y.: Pore Fluid Extraction by Reactive Solitary Waves in 3-D: Reactive Porosity Waves, Geophysical Research Letters, 44, 9267–9275, https://doi.org/10.1002/2017GL074293, 2017.

Pawar, S. and San, O.: CFD Julia: A Learning Module Structuring an Introductory Course on Computational Fluid Dynamics, Fluids, 4, 159, https://doi.org/10.3390/fluids4030159, 2019.

Pusok, A. E., Kaus, B. J. P., and Popov, A. A.: On the Quality of Velocity Interpolation Schemes for Marker-in-Cell Method and Staggered Grids, Pure and Applied Geophysics, 174, 1071–1089, https://doi.org/10.1007/s00024-016-1431-8, 2017.

Qiu, J.-M. and Shu, C.-W.: Conservative High Order Semi-Lagrangian Finite Difference WENO Methods for Advection in Incompressible Flow, Journal of Computational Physics, 230, 863–889, https://doi.org/10.1016/j.jcp.2010.04.037, 2011.

Rackauckas, C. and Nie, Q.: DifferentialEquations.Jl – A Performant and Feature-Rich Ecosystem for Solving Differential Equations in Julia, Journal of Open Research Software, 5, 15, https://doi.org/10.5334/jors.151, 2017.

Räss, L., Simon, N. S. C., and Podladchikov, Y. Y.: Spontaneous Formation of Fluid Escape Pipes from Subsurface Reservoirs, Scientific Reports, 8, 11 116, https://doi.org/10.1038/s41598-018-29485-5, 2018.

Reiner, M.: The Deborah Number, Physics Today, 17, 62–62, https://doi.org/10.1063/1.3051374, 1964.

Riel, N., Bouilhol, P., van Hunen, J., Cornet, J., Magni, V., Grigorova, V., and Velic, M.: Interaction between Mantle-Derived Magma and Lower Arc Crust: Quantitative Reactive Melt Flow Modelling Using STyx, Geological Society, London, Special Publications, 478, 65–87, https://doi.org/10.1144/SP478.6, 2019.

Robert, A.: A Stable Numerical Integration Scheme for the Primitive Meteorological Equations, Atmosphere-Ocean, 19, 35–46, https://doi.org/10.1080/07055900.1981.9649098, 1981.

Scott, D. R. and Stevenson, D. J.: Magma Solitons, Geophysical Research Letters, 11, 1161–1164, https://doi.org/10.1029/GL011i011p01161, 1984.

Shu, C.-W.: High Order Weighted Essentially Nonoscillatory Schemes for Convection Dominated Problems, SIAM Review, 51, 82–126, https://doi.org/10.1137/070679065, 2009.

Smith, C. J.: The Semi-Lagrangian Method in Atmospheric Modelling, Ph.D. thesis, 2000.

Solano, J. M. S., Jackson, M. D., Sparks, R. S. J., Blundy, J. D., and Annen, C.: Melt Segregation in Deep Crustal Hot Zones: A Mechanism for Chemical Differentiation, Crustal Assimilation and the Formation of Evolved Magmas, Journal of Petrology, 53, 1999–2026, https://doi.org/10.1093/petrology/egs041, 2012.

Sonnendrücker, E., Roche, J., Bertrand, P., and Ghizzo, A.: The Semi-Lagrangian Method for the Numerical Resolution of the Vlasov Equation, Journal of Computational Physics, 149, 201–220, https://doi.org/10.1006/jcph.1998.6148, 1999.

Spiegelman, M. and Kenyon, P.: The Requirements for Chemical Disequilibrium during Magma Migration, Earth and Planetary Science Letters, 109, 611–620, 1992.

Spiegelman, M., Kelemen, P. B., and Aharonov, E.: Causes and Consequences of Flow Organization during Melt Transport: The Reaction Infiltration Instability in Compactible Media, Journal of Geophysical Research: Solid Earth, 106, 2061–2077, https://doi.org/10.1029/2000JB900240, 2001.

Staniforth, A. and Côté, J.: Semi-Lagrangian Integration Schemes for Atmospheric Models—A Review, Monthly weather review, 119, 2206–2223, https://doi.org/10.1175/1520-0493(1991)119<2206:SLISFA>2.0.CO;2, 1991.

van Keken, P. E., King, S. D., Schmeling, H., Christensen, U. R., Neumeister, D., and Doin, M.-P.: A Comparison of Methods for the Modeling of Thermochemical Convection, Journal of Geophysical Research: Solid Earth, 102, 22 477–22 495, https://doi.org/10.1029/97JB01353, 1997.

https://doi.org/10.5194/gmd-2023-189
Preprint. Discussion started: 24 October 2023
© Author(s) 2023. CC BY 4.0 License.

Vasilyev, O. V., Podladchikov, Y. Y., and Yuen, D. A.: Modeling of Compaction Driven Flow in Poro-Viscoelastic Medium Using Adaptive Wavelet Collocation Method, Geophysical Research Letters, 25, 3239–3242, https://doi.org/10.1029/98GL52358, 1998.

Wang, R. and Spiteri, R. J.: Linear Instability of the Fifth-Order WENO Method, SIAM Journal on Numerical Analysis, 45, 1871–1901, https://doi.org/10.1137/050637868, 2007.

Yarushina, V. M. and Podladchikov, Y. Y.: (De)Compaction of Porous Viscoelastoplastic Media: Model Formulation: (DE)COMPACTION OF POROUS MEDIA, Journal of Geophysical Research: Solid Earth, 120, 4146–4170, https://doi.org/10.1002/2014JB011258, 2015.

Zerroukat, M., Wood, N., and Staniforth, A.: SLICE: A Semi-Lagrangian Inherently Conserving and Efficient Scheme for Transport Problems, Quarterly Journal of the Royal Meteorological Society, 128, 2801–2820, https://doi.org/10.1256/qj.02.69, 2002.